Hall Thruster Simulations using Particles. I. Discharge Channel

Francesco Taccogna* and Pierpaolo Minelli
*CNR-Nanotec-PLasMI lab, via Amendola 122/D, 70126-Bari, Italy

PACS: 52.65.Rr; 52.75.Di
Keywords: PIC model; Hall thruster; Electron drift instability; Plasma sheath;

There are still many missing elements to complete the physical picture at the basis of the Hall thruster functioning. The origin of the anomalous electron cross-field transport often ascribed to azimuthal electron ExB drift instability remains decoupled from self-consistent ion axial acceleration and radial boundary conditions, at the same time. This study represents the first attempt to correlate the different mechanisms contributing to the electron transport by means of a fully kinetic three-dimensional Particle-in-Cell model. A geometrical scaling scheme has been used to make the simulation possible and a critical assessment of the effects of reducing dimensions has been addressed. The present paper, first of two paired papers, deals with the physics of discharge channel.
Results confirm the occurrence of ExB drift instability along the azimuthal direction. The modulation is almost standing wave: it moves back and forth travelling a short distance before being axially convected away. In addition, the dielectric floating potential nature of the lateral walls gives to the azimuthal modulation an important radial component creating a zigzag pattern. As a consequence, the azimuthal electric field presents a double alternating structure: two phase-opposing waves are present in the first and second half of the radial extension between the two lateral walls. Finally, the effect of secondary electron emission from walls is not sufficient to guarantee the right electron current to neutralize the ion beam, but rather it works as auxiliary mechanism (together with ion heating and azimuthal rotation) to saturate the electron drift instability leading to smaller amplitude oscillations.

*Corresponding author.
E-mail address: francesco.taccogna@cnr.it (F. Taccogna).

I. Introduction

Hall thrusters (HTs) [1-3], also named closed-drift or stationary plasma thrusters, are considered one of the most promising electric propulsion system and it has already been used in different Space missions [4]. It consists of a DC glow coaxial discharge where the anode ring upstream in the channel works as neutral propellant distributor and the external cathode placed in the near-field plume region out of axis works as electron emitter to both sustain the discharge and neutralize the ion beam. The most important feature of HT is its ExB configuration: an almost radial magnetic field peaked at the exit plane of the channel traps the electrons, generating, in combination with the axial field, a closed drift in the azimuthal direction (from now on we will use the nomenclature typical of a cylindrical reference system). Ions, almost insensitive to the magnetic field, fill mainly the effect of the axial accelerating electric field E_z. This configuration guarantees a better ionization efficiency (both by increasing the electron permanence time into the channel and by energize them with the ExB drift) and a better acceleration efficiency (by creating an electron virtual cathode which eliminates the Child-Langmuir current limitation typical of gridded ion thrusters). In the magnetic layer (TML) version, dielectric floating wall materials are used. This guarantees a more extended and gradual acceleration process, while in the anode-layer type (TAL) the walls are made by conductive materials.

One of the most important open questions in the HT physics concerns the electron cross-field mobility. Elementary collisional theory (collision-induced transport CIT):

$$\mu_{CIT} = \frac{\mu_0}{1+h^2} \tag{1}$$

underestimates measured cross-field mobility. Here $\mu_0=q/m\nu$ is the parallel mobility, $h=\omega_{ce}/\nu$ is the Hall parameter, ω_{ce} the cyclotron frequency and ν the electron-neutral momentum transfer (the dominant collisional event) frequency. Experiments [5] have found an axial electron current significantly higher (more than one order of magnitude) than predicted using Eq. (1). The reason for the observed enhanced cross-field transport in HT discharges is nowadays a subject of considerable and continued debate. However, it is well accepted to mainly attribute the anomalous electron transport to two different reasons:

- fluctuation-induced transport (FIT): anomalous axial electron current results from the phase angle correlation between the azimuthal component of the electric field E_θ and density n_e along the azimuthal direction [6, 7]:

$$\mu_{FIT} = \frac{\mu_0 h}{1+h^2} \frac{< n_e E_\theta >}{n_e E_z}.$$

Among the possible origins of this azimuthal modulation, the ExB drift instability [8, 9] due to the large azimuthal electron motion against the practically immobile ions, is considered the one playing the major role. Lafleur et al. [6] have shown that this contribution corresponds to an enhanced electron-ion frictional drag and it is a strong function of almost all plasma parameters (such as electron density n_e and temperature T_e, ion axial $v_{z,i}$ and electron azimuthal $v_{\theta,e}$ drifts, and axial electric field E_z), and consequently, does not simply scale with $\mu_\perp \propto B^{-2}$ or $\mu_\perp \propto B^{-1}$ laws;

- wall-induced transport (WIT): the electron-wall interactions leading to a non-specular

reflection or emission of electrons which leave the walls following another spiral trajectory displaced toward the anode (the so called near-wall conductivity NWC [10]). It leads to an enhanced local collisional-like transport Eq. (1) where the collision is between electrons and lateral walls ($\mu_\perp \propto B^{-2}$). Possible amplifications of this contribution can come from large secondary electron emission from the wall [11, 12] and consequent sheath instability [13-16]. Different measurements [12] have showed that wall material (and in particular secondary electron emission SEE proprieties) has a significant effect on the electron mobility. Nevertheless, it is still not clear if this is a direct or indirect (through for example the electron temperature) effect on the cross-field transport.

Both mechanisms derive their origin from the kinetic character of the electron behavior in HT. In fact, fluid [17] and hybrid models [18-21] of the HT discharge disregard the origin of the anomalous transport and usually invoke an adjustable effective mobility μ_{eff} to achieve electron axial current in agreement with experiments, considered as the result of different independent contributions $\mu_{\text{eff}}=\mu_{\text{CIT}}+\mu_{\text{FIT}}+\mu_{\text{WIT}}$. However, it has been suggested [19, 21, 22] that this way to distinguish different contributions to the mobility with different adjustable coefficients fail to match correctly the ion velocity profile measured by laser-induced fluorescence (LIF) technique. This is a strong argument supporting the conclusion that all the different contributions do not necessarily add each other, but they strongly interfere in non-linear way leading to some kind of total mobility scaling as $\mu_\perp \propto B^{-n}$ with n larger than 2.

The numerical Particle-in-Cell / Monte Carlo Collision (PIC-MCC) [23] attempts to investigate the nature of the anomalous transport can be summarized by 1D radial [11, 12] and 1D azimuthal [9, 24-26] approaches, both unable to correlate FIT and WIT. In particular, both models, due to their reduced dimensionality and geometrical frustration, shows artificially high level of instabilities. Pure radial models show often the appearance of strong beam-plasma, two-stream and sheath instabilities due to the presence of space-charge limited (SCL) sheath regimes characterized by secondary electron emission yield SEY γ larger than the critical value $\gamma_{SCS} = 1 - \sqrt{2\pi\mu}$, where $\mu = \frac{m}{M}$ is the electron to ion mass ratio ($\gamma_{\text{SCS}}\approx 0.985$ for Xe). Pure azimuthal models show the presence of ExB drift instability characterized by large values of amplitude azimuthal oscillations of electron density and azimuthal electric field.

A step forward was accomplished by 2D radial-azimuthal [27-30] approaches that have confirmed the non-linear interplay between FIT and WIT to produce the total axial electron current. Nevertheless, in these models, the accelerator axial electric field E_z is externally imposed while, one expects that an increase of the local conductivity due to the anomalous transport would lead to a decrease of the local electric field, which in turn would reduce the electron azimuthal drift and dump possible instabilities which have triggered the anomalous mobility itself. Furthermore, the limitation due to the missing inclusion of the axial coordinates has been banned by Héron and Adam [28] who showed that, on a time scale smaller than 1 μs (i. e. the ion transit time across the discharge channel), the current can reach very large values, and by Lafleur et al. [25] and Hara et al. [30] who showed how an artificial axial boundary condition can strongly influence the final results.

In the same way, 2D azimuthal-axial models [8, 31-33] unavoidably ignore the radial direction and any possible contribution and/or saturation mechanism represented by the electron-wall interaction. Furthermore, collective Thomson scattering experiment [34] has shown that in the

thruster channel the azimuthal mode has a wave vector with significant non-vanishing component along the magnetic field (5 degrees deviation from the azimuthal direction), making the radial direction important not only in relation to pure WIT. As further proof of the influence of the radial walls on the azimuthal drift, Lafleur et al. [6] have shown that the finite size of radial extension (in the SPT100 $\lambda_D/\Delta r \approx 0.05$, where Δr represents the channel width) modifies the resonant comb-like nature of the dispersion relation towards linear one (modified ion-acoustic type instability). This characteristic has also been observed in experiments [35, 36] and known as electron demagnetization mechanism [26].

These characteristics and in particular the complex interplay among all the three directions make a fully kinetic three-dimensional representation necessary. Curiously, the first 3D kinetic attempt to model HT, dates back to 90's by the pioneering works of Hirakawa and Arakawa [37, 38] who applied PIC-MCC technique to a SPT50 using fake values of ion mass (smaller) and vacuum permittivity (larger). These tricks, often used also in recent simulations [31], would irremediably and irreversibly affect the electron transport inside the channel. Differently, in the present study, we concentrate our efforts to represent the HT plasma in the full three-dimensional domain by means of a Particle-in-Cell / Monte Carlo (PIC-MCC) methodology without changing any fundamental physical constants. The aim of this work is to assess the different contributions to the anomalous transport (the investigation methodology undertaken provides the ability to isolate separately wall and azimuthal contributions) and to show if and how azimuthal fluctuations and radial plasma-wall interaction work together to create the extra cross-field transport mechanism with the consequent modification of the axial electric field structure. This work consists of two companion papers. In this first paper, the region investigated is the channel discharge from the anode to the exit plane, while the second paper [39] deals with the near-field region of the plume (NFP). The model is presented in detail in section II, where the geometrical scaling used to alleviate numerical constraints and to speed up the execution of the code while keeping the main HT physical mechanisms almost unchanged is presented and its limitation/validity discussed. Section III is devoted to the presentation and discussion of results.

II. Numerical Model: Description, Assumptions and Limitations

This section is dedicated to the description of the numerical model pointing out all the approximations done. Far from being limited, these allow for sorting of phenomena to be detected and to be out of investigation. This represents a strong point in favour of simulations that otherwise would become mere reproduction of experiments which instead are rather limiting in isolating the individual mechanisms involved in a complex physical framework. In fact, HT is a very complex plasma device: the number of possible waves and instabilities is very large [40] and the range of spatial and temporal scales of different phenomena involved is quite wide. Due to the first principle nature of PIC model, its results could be difficult to interpret if one does not limit by purpose the description. Within this model, we restrict our investigation to short wavelengths and high frequencies phenomena without including the neutral dynamics and electromagnetic induction but reproducing the interaction between azimuthal drift instability, radial plasma-wall interaction and axial acceleration.

The computational technique used is the standard Particle-in-Cell/Monte Carlo Collision (PIC-MCC) model. The three-dimensional model represents an extension of previous low-dimensional ones [11, 41, 27]. The domain corresponds to a typical coaxial HT channel limited axially by the anode and the exit plane and radially by the inner and outer walls. Only a sector

(a quarter) is retained in the azimuthal direction because of computational time considerations. Periodic boundary conditions are imposed along the latter direction, both for particles and fields quantities. We have decided to use a cylindrical metrics in place of Cartesian one in order to reduce the number of cells necessary to cover the computational domain. The onset of possible numerical heating due to self-force [42] induced by non-uniform cells can be excluded due to the fact that inner radius is much smaller than the channel width and that the cell is only weakly deformed. The equations of motion (EOM) in cylindrical coordinates are solved with the leap-frog/Boris algorithm using the Boris prescription [43]: EOM are solved in a local Cartesian reference system and then Cartesian to cylindrical transformations are applied to radial and azimuthal coordinates. The new radial and azimuthal components of the velocities are projected (by simple rotation) in the new local Cartesian reference frame pointing to the new particle position. In this way, we avoid directly solving the intrinsically non-linear (due to the presence of inertial forces) EOM in cylindrical coordinates. The radial centrifugal force necessary to support the circular electron motion in closed azimuthal orbits and coming from the radial magnetic field is automatically taken into account [44].

In place of reducing the vacuum permittivity or the ion mass, a geometrical scaling [45] derived from HT miniaturization technology has been applied: every dimension is reduced by f keeping constant all the most relevant non-dimensional Knudsen and Hall parameters (magnetic field and neutral density are increased by a factor f). As a consequence, the electron current injected from the cathode is reduced by f^2 in order to keep the same current density. Considerations related to the validity of self-similar HT plasma physics under geometrical scaling will be presented in the dedicated Sec. II.a.

A prescribed axial distribution of neutral Xe atom density (drop of two orders of magnitude from the anode to the exit plane) while uniform in radial and azimuthal directions, taken from [46] is kept fixed during all the simulation. This excludes from the possible phenomena investigated those related to the neutral dynamics as low ~kHz frequency breathing mode [47] and rotating spoke [48].

The model is electrostatic (only Poisson equation is solved). The magnetic field map (radial and axial components) is fixed during the simulation and taken from [18]. Therefore, possible magnetic field fluctuations that have been shown [49, 50] additionally enhancing the electron transport across the magnetic field lines, have been ignored.

The simulation starts from an empty domain. Electrons are introduced every time step from the exit plane (distributed following the cylindrical uniformity) sampling their velocity from a half-Maxwellian distribution (the temperature T_{e0} chosen in order to take into account the energy gained in the NFP region, as from NFP experimental measurements [51] and model results from the companion paper [39]). The amount of electrons injected inside the channel every PIC iteration is determined by subtracting the un-neutralized ion current exhausted from the current discharge $I_{e,inj}=I_d-(I_{beam}-I_{e,ep})$. Poisson equation in three-dimensional cylindrical geometry:

$$\left(\frac{\partial^2}{\partial r^2}+\frac{1}{r}\frac{\partial}{\partial r}+\frac{1}{r^2}\frac{\partial^2}{\partial \theta^2}+\frac{\partial^2}{\partial z^2}\right)\phi(r,\theta,z)=-\frac{\rho(r,,z)}{\varepsilon_0} \tag{2.a}$$

is solved with PETSc software package [52]. For this purpose, Dirichelet fixed conditions are used on axial borders at $z=0$ (anode) and $z=z_{ep}$ (exit plane):

$$\phi(r,\theta)\rfloor_{z=0}=V_d, \tag{2.b}$$
$$\phi(r,\theta)\rfloor_{z=z_{ep}}=V_{ep}, \tag{2.c}$$

while the floating potential on the lateral walls is self-consistently obtained neglecting the electric field inside the material and imposing the resulting Neumann condition:

$$\left.\frac{\partial\phi(\theta,z)}{\partial r}\right|_{r=r_{out/in}} = \mp\frac{\sigma(\theta,z)}{\varepsilon_0} \tag{2.d}$$

where the sign – and + is for the outer r_{out} and inner r_{in} wall, respectively. The potential at the exit plane has been fixed at an intermediate value V_{ep} between the anode V_d and the cathode V_c=0 levels, taken from different works [46]. Nevertheless, note that the imposition of a fixed voltage condition at the exit plane dump all the azimuthal modulations there.
Concerning particle-wall interactions, when an electron hits the lateral dielectric surface, a Monte Carlo probabilistic model [53] is used to choose the number of electrons emitted SEY γ based on the energy E_p of the primary impacting electron. It distinguishes among three different types of secondary electrons emitted: a) backscattered electron, if no energy is lost and just the radial velocity is reversed; b) re-diffused electron, if the primary electron penetrates inside the material and suffers inelastic collisions before reemitted (Augier electron); c) true secondary electrons, if the primary electron is lost inside the material and induces emission of electrons (even more than 1) belonging to the material with a temperature T_e=T_{see}. A lack of data is still present in the low energy range E_p<10 eV: a value of γ_0= $\gamma(E_p$=0) = 0.55 and E_p^*=$E_p(\gamma$=1) = 44 eV have been used simulating the typical SEY proprieties of Borosil. The energy dependence of different contributions to the total SEY is reported in Fig. 1. It should be pointed out that results are very sensitive to γ_0 and even more to E_p^* chosen. This is because the average energies with which electrons collide the two lateral walls in the acceleration region have been computed to be about $\langle E_p\rangle_{in/out}$≈20 eV. No dependences from the angle of impact (important only for E_p>100 eV) and from wall temperature have been taken into account, even if recent experiments [54] show that BN-SiO_2 SEY decreases (γ_0 decreases while E_p^* increases) with increasing wall temperature. The time scale investigated is too small to take into account possible wall temperature evolution. Finally, when an ion strikes the walls it is neutralized and deleted from the list of particles tracked.

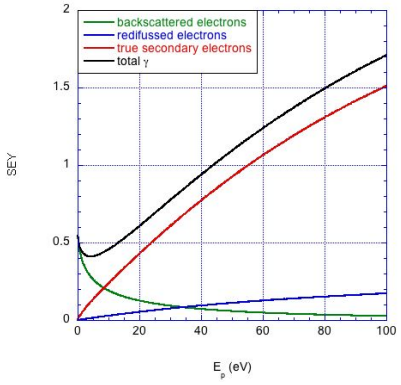

Fig. 1 – The different contributions to the total SEY γ as a function of the impacting energy of the primary electron. Data corresponds to BN-SiO2 material.

When electrons and ions leave the simulation domain from anode and exit planes at z=0 and z=z_{ep}, respectively, they are deleted from the list and a counter stores the number of particles in order to compute anode and beam currents.

We apply the standard "null collision" Monte Carlo technique [55] to simulate electron-neutral (Xe) collisions, which include elastic scattering, excitation, and single ionization (cross sections taken from ref. [56]). Recently, it has also been suggested that the apparent discrepancy between classical and anomalous electron transport could be caused by an underestimation of ion current in simulations and experiment due to neglecting Xe^{++} doubly charged ions [57]. For this reason, we have added collisions producing Xe^{++} ions such as direct double ionization of Xe atoms [58] $e + Xe \rightarrow 3e + Xe^{++}$ and single ionization of Xe^{+} ions [59] $e + Xe^{+} \rightarrow 2e + Xe^{++}$. All ions generated from neutral ionization inherit a velocity sampled from a Maxwellian distribution at the temperature T_N. Finally, Coulomb and ion-neutral collisions have been neglected. The firsts are considered to have a weak effect in comparison to instability-enhanced electron-ion friction while the seconds are too weak to possibly dump electron drift instability [7].
Hybrid parallel programing techniques for multicore architectures with distributed and shared memories have been implemented using a combination of Open Multi-Processing (OpenMP) and Message Passing Interface (MPI) commands.

II.a Considerations on the geometrical scaling

The first step consisted to verify the quality of the geometrical scaling. The value of the scaling factor chosen f=10 guarantees plasma still to be globally neutral. A larger scaling factor would approach the lateral sheaths much closer and the system would become surface-dominated: the aspect (surface to volume) ratio is unavoidably changed under geometrical scaling. All the most relevant HT plasma parameters (potential ϕ, plasma density n_p, electron temperature T_e, electric axial field E_z, azimuthal electron $v_{e,\theta}$ and axial ion $v_{i,z}$ drifts) computed within the scaled model have been reported in Figs. 2, where axial profiles at the channel centerline r_m and averaged along the azimuthal direction and over a total time of 0.2 μs have been compared with data measured and results obtained by different models [17, 22, 46]. The agreement is very good and a slight discrepancy is only observed close to the exit plane due to the artificial boundary condition imposed there. The axial profiles allow to clearly identify the two characteristic regions of HT channel discharge: the anode-ionization (from z=0 to about the maximum of the plasma density at z_{ion}=16 mm) and the acceleration (last 8 mm) regions.

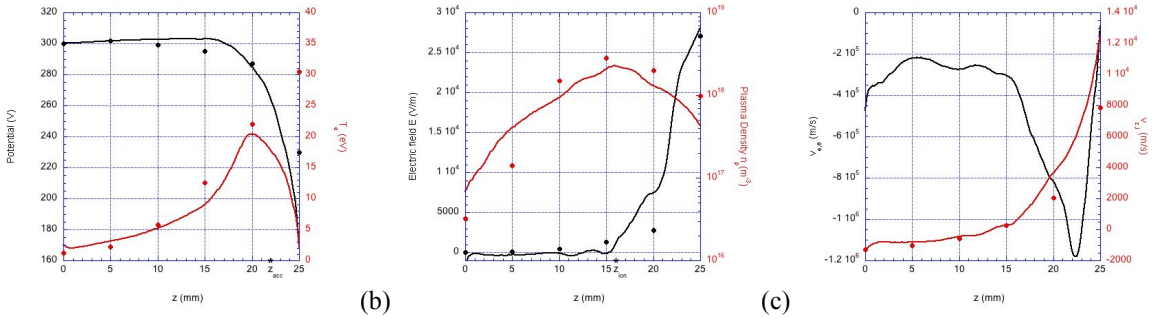

(a) (b) (c)

Fig. 2 – Axial profiles of (a) potential (in black) and electron temperature (in red), (b) accelerator electric field (in black) and plasma density (in red) and (c) azimuthal electron (in black, negative since electrons drift in the anticlockwise direction) and axial ion (in red) drifts as computed with the present geometrically scaled (f=10) model (full lines) and compared with available measurements and results from different models (circles) [17, 22, 46]. The axial length z and axial electric field E_z have been rescaled to the real value (i.e. z has been multiplied by f while E_z divided by f) in order to have unscaled values for comparison with experimental/model results. All the profiles are calculated along the channel centerline r_m and averaged along the azimuthal direction and over 10^5 PIC cycles (0.2 μs, corresponding to the wave amplitude oscillation).

TABLE I. Scaling laws of the most representative HT plasma parameters.

Quantity	Symbol	Scaling law
Debye length	λ_D	f^0
Electron Larmor radius	ρ_L	f^1
Gradient length	l_∇	f^1
Electron, ion frequencies	ω_{pe}, ω_{pi}	f^0
Electron-neutral collision frequency	ν_{eN}	f^1
Electron-wall collision frequency	ν_{eW}	f^1
Electron cyclotron frequency	ω_{ce}	f^1
Electron ExB drift velocity	v_{de}	f^0
Diamagnetic, gradient-B drift velocities	v_∇	f^0
Ion beam velocity	v_{di}	f^0
Convection time	τ_c	f^1

In Table I, the scaling laws of the most relevant HT parameters have been reported: Debye length, electron and ion frequencies, ion sound speed, electron drift, ion beam velocity, all remain unchanged. Taking into account the useful relations obtained by Lafleur et al. [6, 7] on ExB drift instability (threshold conditions for the onset, wave number, frequency, amplitude and growth time), one should expect to faithfully reproduce the azimuthal modulation and as a consequence the FIT. The possible changes may concern the reduced convection time τ_c (that however still remain larger than the instability grow time τ_g with the scaling factor chosen, since $\tau_g/\tau_c \approx \omega_{ce}/\omega_{pe}$ [7]), the channel length that still remains larger than the scale length for wave growth (estimated to be about 0.25 mm in ref. [60]) and the azimuthal to axial electric field components ratio E_θ/E_z (the amplitude of the azimuthal field, depending from electron density and temperature, remains unchanged, while the axial component increases by a factor f).

It remains to consider the effects of the parameters that directly change under geometrical scaling: the electron Larmor radius, the gyrofrequency, the gradient length-scales and the electron-wall collision frequency.

Even if, the ratio between Debye length λ_D and electron Larmor radius ρ_L increases by a factor f, the relation $\lambda_D << \rho_L$ is still valid with f=10. This allows using the same simplified dispersion relation derived based on the large gyroradius limit obtained for the real size HT. At this concern, it should be noted that under geometrical scaling, $l=\lambda_D/\Delta r$ increases by f. This guarantees that the linear nature of the dispersion relation is also kept in the reduced size thruster. In addition, with f=10, the ratio $\lambda_D/2\pi r$ is still large enough to guarantee that the azimuthal spectrum remains essentially continuous.

While the ratio between electron cyclotron angular ω_{ce} and collisional ν frequencies, i.e. the Hall parameter $h=\omega_{ce}/\nu$ is unchanged, the two quantities increase by a factor f under scaling. In particular, Cavalier et al. [61] have shown that the resonance nature of the dispersion relation is higher for larger gyrofrequencies. This effect could be compensated by the introduction of a radial component on the wave which in turn sharpen the resonances.

Even if the gradient B and diamagnetic drifts remain unchanged under geometrical scaling (that is ExB remains the dominant drift by a factor larger than 20), the typical gradient length of magnetic field, density and electron drift (related to the shear rate [62]) are smaller by a factor f. This reduction can trigger Rayleigh instability in the scaling model. They have already been predicted and observed in a 900 W HT [63, 64] as high-frequency (1-50 MHz) azimuthal mode with phase velocity close to the electron drift velocity.

Finally, we expect to see a larger contribution of the WIT due to the larger electron-wall collision frequency. Differently from FIT, WIT can be easily controlled. If no space-charged saturation or sheath instability are triggered, this effect is simply linear and local (equivalent to

a near-wall CIT). In addition, its ratio with the electron-neutral collision frequency is unchanged leading to a classical transport contribution kept balanced between volume and near-wall effects.

III. Results

The operative conditions simulated (typical of a SPT100 HT configuration [3] scaled with f=10) and numerical parameters used in the model have been reported in Table II.

Table II. Typical operating corresponding to a SPT100 [3] (scaled with f=10) and numerical parameters used in the PIC simulations.

Quantity	Symbol	Value
Channel length	z_{ep} (scaled)	2.5 mm
Inner radius	r_{in} (scaled)	3.45 mm
Outer radius	r_{out} (scaled)	5 mm
Anode voltage	V_a	300 V
Exit plane voltage	V_{ep}	170 V
Discharge current	I_d (scaled)	4.5×10^{-2} A
Magnetic field peak	B_{max} (scaled)	1800 G
Electron temperature from exit plane	T_{e0}	20 eV
Secondary Electron temperature	T_{see}	2 eV
Neutral density at anode / exit plane	$n_{N,a}$ / $n_{N,ep}$ (scaled)	2×10^{20} / 3×10^{19} m^{-3}
Neutral temperature	T_N	700 K
SEY at E_p=0	γ_0	0.55
SEY first crossover energy	E_p^*	44 eV
Cell size	∇z	15 μm
Time step	∇t	2×10^{-12} s
Averaged number of particles per cell	N_{ppc}	80

The cell size (uniform along all directions) turns out to be smaller than the minimum Debye length (λ_D=15.4 μm at z=z_{ion} as it can be seen in Figs. 2) measured during the simulation. It gives a mesh with N_rxN_θxN_z=101x129x161 nodes. The time-step is chosen such that $\omega_p \Delta t$=0.3, where again ω_p is the maximum plasma frequency detected. A total number of PIC cycles $N_{PIC}=2.5 \times 10^6$ (corresponding to t=5 μs) have been last before producing steady state results (even if a quasi-stationary state is reached already after 0.5 μs). The particle weight $w=10^3$ used gives a total number of $N_p=2 \times 10^8$ electrons/ions at the end of the simulation. All the quantities plotted (profiles or two-dimensional maps) are averaged over 250 time steps (i.e. 0.5 ns) during the maximum wave amplitude phase. Double ionized ions result smaller than 5% of the total ion population.

III.a Radial asymmetry and cylindrical metrics effects

It is worthwhile noting that all the theoretical treatments [6, 61] of electron ExB drift dispersion relation and different numerical models [9, 12, 24, 25, 29, 30] neglect the cylindrical curvature and use the Cartesian approximation.

As shown in Fig. 3, the radial profiles (calculated in the acceleration region at z=z_{acc}, indicated in Fig. 2.a, and averaged along the azimuthal direction) of plasma potential and electron/ion density show a high level of symmetry between inner and outer walls. This is a proof that the Cartesian metrics is a good approximation due to the low $r_{in}/\Delta r$ value (preserved in the geometrical scaled model). In order to confirm this result, in the same Fig. 3, the corresponding quantities obtained with the Cartesian (x,y,z) version of the code have been reported. In the

Cartesian version, the coordinate x corresponds to the radial coordinate, while y represents the ExB direction and its length is fixed to $\frac{\pi}{2} r_m$, where periodic conditions are imposed. The HT turns into a parallelepiped infinitely long in the y direction. The Cartesian version of EOM and Poisson equation are solved. The inner and outer values of the wall potential, surface charge density and electron/ion densities are approximately the same. In addition, the peak is centered in the middle between inner and outer walls.

The second most evident result is that the lateral sheaths show monotonic drops. No SCL regimes (even only transiently) have been detected all along the simulation and the SEY takes values of about $\langle\gamma\rangle = \int \gamma(E) f(E) dE = 0.7$ in the acceleration region, far below the critical SCL value. However, it is sufficient to reduce the value of E_p^* by 10 eV for triggering temporally intermittent double-layer structures in the sheaths of the acceleration region. For even smaller E_p^* values, steady state inverse sheath regime has been relieved. However, a recent work [54] on BN-SiO_2 material has demonstrated that, with wall temperature of 600 K (usually reached in the acceleration region of HT [65]), E_p^* cannot be smaller than 70 eV. Therefore, one can exclude the occurrence of SCL or inverse sheath regimes in HT steady state operation.

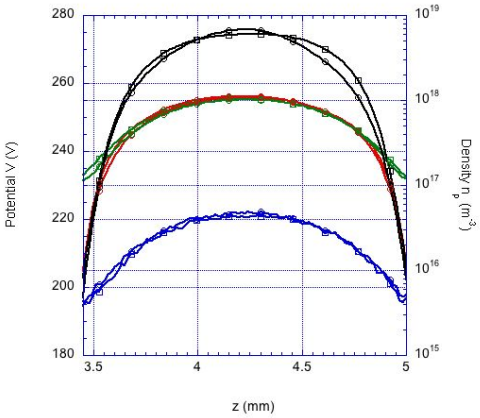

Fig. 3 – Radial profiles of potential (black curves), electron (red curves), Xe^+ (green curves) and Xe^{++} (blue curves) ion densities using cylindrical (circles) and Cartesian (squares) metrics.

III.b Axial behaviour of the azimuthal drift instability

Figs. 4 show two-dimensional maps in the (θ,z) plane at the thruster centerline r_m of potential, azimuthal electric field and electron density at the instant of maximum wave amplitude. The wave is well defined along the entire length of the discharge channel with a larger fluctuation amplitude in the acceleration region. Shorter wavelength structures are evident in the ionization region overlapped with a large wavelength modulation towards the anode region. As demonstrated by ExB drift instability theory, the wavelength of the fluctuation is proportional to Debye length and then it changes with electron density and temperature along the channel (see Figs. 2.a and 2.b). The wavenumber shows a small axial component. The maximum amplitude of the plasma potential fluctuation $\delta\phi$ is about 10 V, corresponding to $T_e/2$, while the amplitude of the azimuthal electric field oscillations reaches a maximum of 3×10^4 V/m in the acceleration region, i.e. ten times smaller than the axial component there (we remind the reader that, under geometrical scaling the electric field E_z is ten time larger than in the real size thruster). The amplitude of the plasma density fluctuation at its maximum reaches about 20% of the average plasma density.

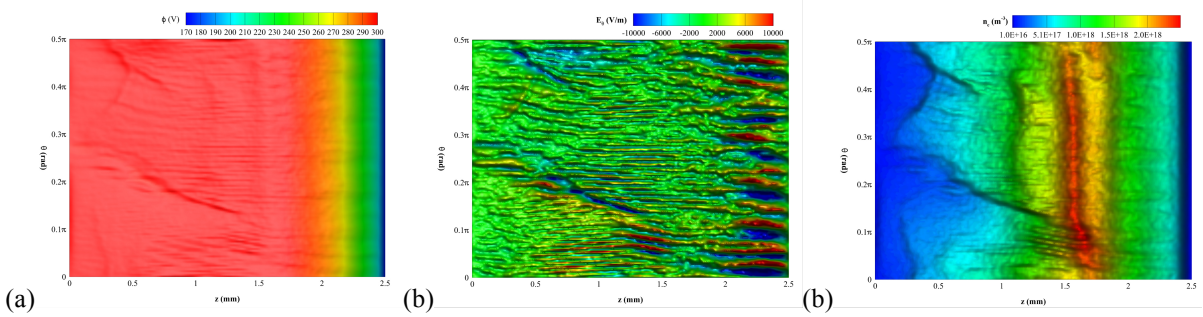

Fig. 4 - Two-dimensional maps in the (θ,z) plane at r=r_m of (a) potential, (b) azimuthal electric field E_θ (V/m) and (c) electron density n_e (m^{-3}) at the instant of maximum wave amplitude.

Fig. 5 shows the azimuthal profile of the electric potential at r=r_{in}+Δr/3 and z=z_{acc} at six different times during the instability. The total period ΔT_{ampl}=0.2 μs corresponds to the ion convection time that, in the scaled model (reduction of the acceleration region), is characterized by a larger frequency (about 5 MHz) respect to the real size thruster [66]. During the instability, the wave shakes back and forth in the ExB direction with a phase velocity of v=4000 m/s (corresponding to an ion acoustic wave at T_e=20 eV). It results in an almost standing wave due to the fact that the azimuthal extension covered is very short. Even during the quiescent phase, a small modulation, whose amplitude is about 4 V, is always present. Of course, the amplitude and period are modified by the geometrical scaling of the thruster and further investigations need to evaluate their changes with the real size thruster.

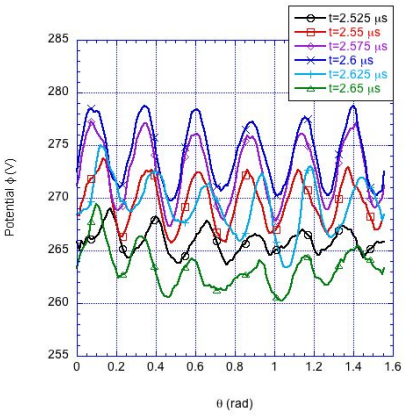

Fig. 5 – Azimuthal profile of the electric potential at r=Δr/3 and z=z_{acc} have been reported at different times during the amplitude oscillation period.

However, the characteristic of standing wave has been experimentally observed [36] and it is compatible with the presence of erosion patterns (known as anomalous erosion) at the walls [67]. Already in previous models [25], this has been indicated as being due to the fact that the instability travels just a very short distance before being axially convected away.

III.c Coupling between azimuthal drift instability and lateral radial plasma-wall interaction in the acceleration region

In order to study the correlation between azimuthal and radial dynamics, we are reporting in Figs. 6 the two-dimensional maps of potential, azimuthal electric field and electron density in the (r,θ) plane at z=z_{acc}. Again, the snapshot corresponds to the moment of maximum wave

amplitude. The dominant component of the modulation is characterized by a wavelength $\lambda \approx 1$ mm, in good agreement with ExB drift instability theory and experimental measurements.

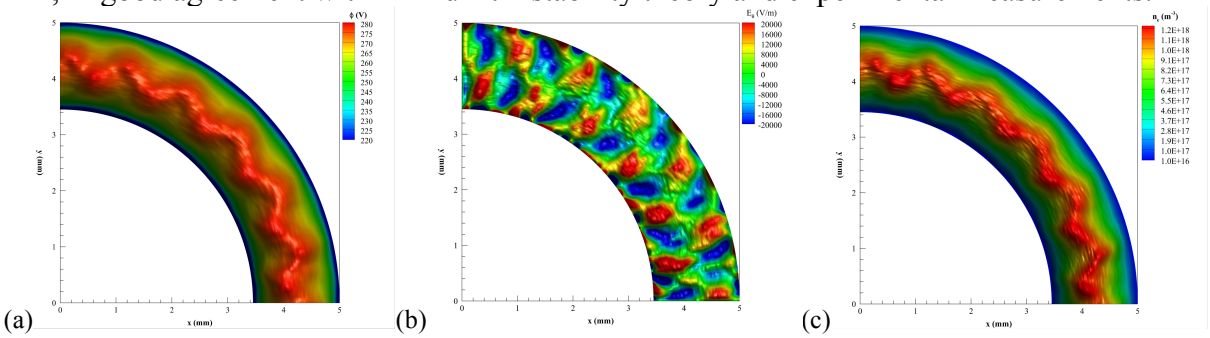

Fig. 6 - Two-dimensional maps in the (r,θ) plane in the acceleration region at $z=z_{acc}$ of (a) potential, (b) azimuthal electric field E_θ (V/m) and (c) electron density n_e (m^{-3}) at the instant of maximum wave amplitude.

The most noticeable result is the multidimensionality character of the modulation: it is not purely azimuthal but it has a marked radial component (amplified by the geometrical scaling that brings the lateral walls close together). The potential and electron density fronts are tilted showing a zigzag pattern in agreement with Hara et al. 2D(r,θ) model results [30]. As a consequence, the azimuthal electric field presents a double alternating structure: two phase-opposing waves are present in the first and second half of the radial extension between the two lateral walls.

The radial shaping of the wave is due to the coupling between the ExB driven sound wave in the plasma bulk with the floating boundary conditions (Eq. (2.d)) on the lateral dielectric walls (Simon short circuit). Bulk modulation creates preferential azimuthal locations for current closure at the walls, inducing an azimuthal modulation of the sheath. This in turn represents a positive feedback for the ion sound bulk instability. In fact, as already observed in previous works [13, 15, 16], the floating dielectric walls provide a reactive response: the reflection of the tilted standing wave on the walls sustains its generation. As a consequence, the electron radial flux in the same (r,θ) plane, reported in Fig. 7, shows an azimuthal channeling: the direction of the flow is alternatively oriented towards the inner and outer walls. We have verified that using metallic walls (fixed potential boundary conditions on the lateral surfaces) this structure does not appear.

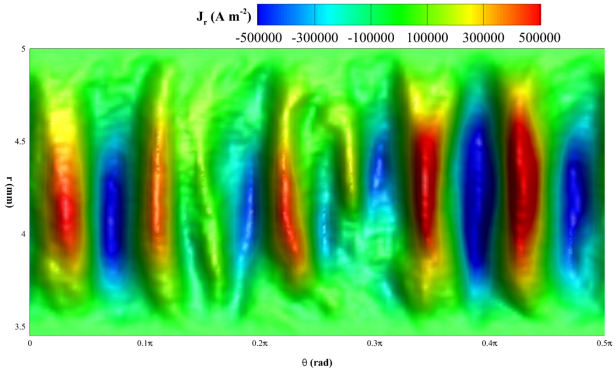

Fig. 7 - Two-dimensional maps in the (r,θ) plane in the acceleration region at $z=z_{acc}$ of the radial component of the electron current density $j_{e,r}$ (A/m^2) at the instant of maximum wave amplitude.

Therefore, for the dielectric walls, both lateral sheaths result azimuthally modulated: they lose their mono-dimensional character and become two-dimensional structures. The sheath modulation creates preferential paths for electrons/ions to move from one wall to the other at certain azimuthal locations. In order to remark the fact that the modulation arrives up to the surfaces, plots of the surface charge density on the inner and outer walls have been produced in Figs. 8. Reminding that the modulation is practically a standing wave, the anomalous erosion can be correlated to locations on the wall characterized by high surface negative charge density. These sites represent preferential points for the ion collection and erosion.

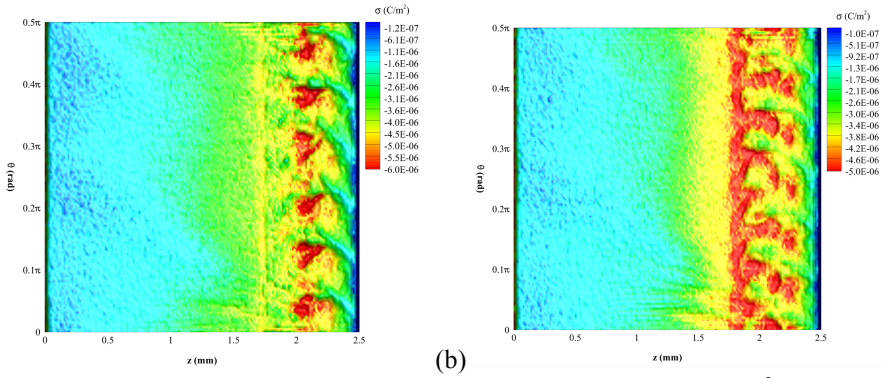

Fig. 8 - Two-dimensional maps in the (θ,z) plane of the surface charge density σ (C/m^2) (a) at the inner and (b) outer walls, at the steady state.

III.d FIT and WIT contributions to the electron transport

This paragraph is devoted to assess the single contribution to the anomalous transport. For this purpose, two cases have been launched in addition to the general one (3D with SEE named CASE 1): a case (CASE 2) without secondary electron emission from the wall (all the electrons arriving at the lateral surfaces are absorbed without inducing any secondary electron emission), and another case (CASE 3) with secondary electron emission module active again, but 2D(r,z) imposing the azimuthal uniformity (achieved by reducing the number of nodes along the azimuthal direction to only two and imposing periodic conditions on both nodes). In the first case, one expect to find the pure FIT of the electrons across the magnetic field lines, while in the second case, only WIT is present. In this way, we have the possibility to compare the case when both the mechanisms are present at the same time, with those where every single mechanism without the contamination of the second one is active. In Table III, some global quantities for the different cases have been reported. The most apparently surprising result is that the ratio between the electron current entering the channel and the ion beam current exhausted $I_{e,inj}/I_{i,beam}$ is not maximum in the general CASE 1 (when all the contributions are at work) but rather in the CASE 2, when the walls are non-emissive. However, this ratio is well above (two times larger) the experimental value of 0.2-0.3 [3, 57], due to the strong condition imposed on the exit plane and the missing inclusion of the NFP in the simulation domain.

In particular, Fig. 9 shows the axial component of the electron current density $j_{e,z}$ flowing towards the anode as a function of the axial location for the three different cases. The value has been computed averaging the electron density and axial velocity along the azimuthal (for CASE 1 and 2) and radial directions. Comparing the two 3D cases, the current computed without SEE (CASE 2) is always larger than the case with SEE in the entire acceleration region. The reason is due to the fact that electron drift instability shows larger amplitudes with non-emissive walls, i.e. secondary electron emission works as an additional saturation mechanism for the electron drift instability. It is also evident how SEE works as an electron thermostat. Two third of the

electron current flowing in the acceleration region reaches lateral walls and 70% of this current is refreshed with cold secondary electrons. This result is in agreement with a recent experiment [68] that has measured higher electron current density with carbon velvet (zero-electron emission) wall material. This would also explain the large values of oscillation amplitudes found in pure azimuthal models [25] that do not take into account secondary electron emission.

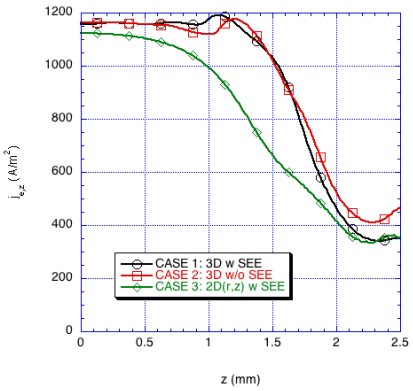

Fig. 9 – Behavior of the axial component of the electron current density $j_{e,z}$ (A/m^2) along the discharge channel for the three different cases launched: CASE1 - 3D with secondary electron emission (black curve with open circles), CASE 2 - 3D without secondary electron emission (red curve with open squares) and CASE 3 - 2D axial symmetric with secondary electron emission (green curve with open rhombus).

The pure SEE CASE 3 (no azimuthal fluctuations active) gives an axial cross-field electron current always smaller and very close to the general CASE 1 only in the last part of the acceleration region. However, analyzing it in detail, the CASE 3 results highly dynamic. It is characterized by strong axial oscillations of the accelerating field which helps to increase the axial electron current necessary to neutralize the ion beam current. This longitudinal oscillation (reported in Fig. 10 the potential at three different axial locations as a function of time), characterized by a frequency of ν=1.25 MHz, corresponds to a resistive instability that have been already observed in hybrid models [69] when the electron axial mobility is low. Such a mechanism, absent in the full 3D CASE 1, replaces the ExB drift instability in producing the right amount of axial electron current, being WIT alone not sufficient to guarantee the necessary electron current.

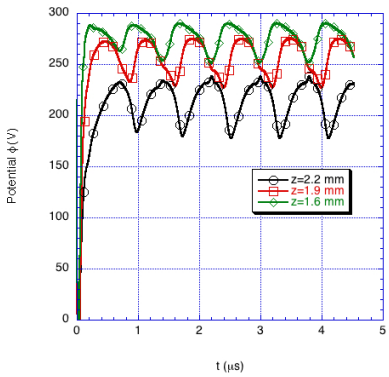

Fig. 10 – Temporal evolution of plasma potential at three different axial location in the CASE 3.

Table III – Quantities computed for three different cases launched. For CASES 1 and 2, values are averaged over ΔT=0.2 μs, while for CASE 3 values are averaged over ΔT=0.8 μs.

Quantity (scaled values)	CASE 1: 3D(r,θ,z) w SEE	CASE 2: 3D(r,θ,z) w/o SEE	CASE 3: 2D(r,z) w SEE
Electron current injected at exit plane $I_{e,inj}$ (x10^{-2} A)	1.4	1.9	1.4
Ion beam current $I_{i,beam}$ (x10^{-2} A)	3.1	2.6	3.1
Electron current at r_{in} $I_{e,in}$ (x10^{-2} A)	0.43	0.15	0.24
SEY at r_{in} γ_{in}	0.64	/	0.66
Electron current at r_{out} $I_{e,out}$ (x10^{-2} A)	0.65	0.2	0.41
SEY at r_{out} γ_{out}	0.67	/	0.71
Max electron temperature $T_{e,max}$ (eV)	20	21	20
Max Potential fluctuation amplitude $\delta\phi_{max}$ (V)	10	15	/
Max density fluctuation amplitude $(\delta n/n)_{max}$	0.23	0.33	/

III.e Evolution, Saturation of the ExB Drift Instability: Distribution Functions

In this paragraph, we report on the nonlinear evolution of the ExB drift instability. We confirm the three stages evolution already observed by Lampe et al. [70] (the ω_{ce}/ω_{pe} ratio used there is similar to that in the geometrical scaled model). After the quasilinear development of the ExB drift instability (not shown) characterized by a small wave number plasma wave, the plasma-wall interactions flatten the individual cyclotron resonances, and the instability becomes ion acoustic-like. The resulting electron heating is evident from the corresponding velocity distribution function EVDF. Fig. 11 shows in particular the azimuthal and radial components (full red and black curves, respectively) computed exclusively for those electrons present in the acceleration region (last fifth of the discharge channel). These curves demonstrate that the heating is purely azimuthal, while there is no visible deformation of the distribution function in the radial and axial directions. The latter are well fitted by a one-Maxwellian distribution function (broken black curve in Fig. 11) with a temperature close to the initial one used to inject electrons from the exit plane $T_{e,r}\approx T_{e,z}\approx T_{e,0}$=20 eV. A small deviation for the radial projection is due to the effect of the depleted loss cone determined by high-velocity electrons. These tails of EVDF contain electrons with radial energy sufficient to overcome the lateral sheath potential barriers. In the ExB direction, the EVDF is much better represented by a bi-Maxwellian distribution function (broken red curve in Fig. 11): the dominant (about 80%) hot component is drifting with $v_{de}\approx$-1.4x10^6 m/s (in the model electrons rotate in the anticlockwise direction) shows a temperature $T_{e,\theta h}$=26 eV, while the remaining cold component is characterized by $T_{e,\theta c}$=7 eV. This heating is one of the most striking features of the electron ExB drift instability.

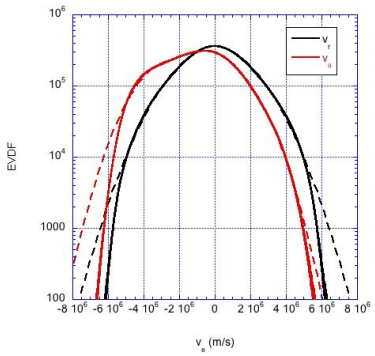

Fig. 11 – Electron velocity distribution function for radial (black) and azimuthal (red) components with the best fitting represented by bi-Maxwellian distribution (corresponding broken lines). Results corresponds to electrons located at z=z_{acc}.

The ion acoustic instability then evolves quasi-linearly until the fluctuating electric field reaches values large enough to heat up and trap ions. The signature of ion trapping has been revealed by the azimuthal component of the Xe^+ ion current density in the (r,θ) plane at $z=z_{acc}$ shown in Fig. 12.a. It reflects the structure of the azimuthal electric field in the same plane (Fig. 5.b). Moreover, the enhanced electron-ion collisions (responsible for the anomalous transport) induce by friction an ion rotation along the ExB in the same direction of electron rotation. Both, ion heating and azimuthal rotation are evident from the azimuthal component of the ion velocity distribution function IVDF represented in Fig. 12.b with black line in logarithmic scale (left vertical axis). As for the electrons, the ions are well fitted by a bi-Maxwellian distribution function characterized by a dominant low temperature component with $T_{i,\theta,c}$=1500 K and a hot temperature component characterized by $T_{i,\theta,h}$=8000 K and an azimuthal drift of $v_{di,\theta}\approx$-4000 m/s. The ion azimuthal drift velocity computed is in good agreement with theoretical prevision and recent models [7, 32], while the percentage of drifting ions is much smaller due to the fact that the ion convection time is reduced in the geometrical scaled model. No cathode location or spoke instability (both neglected in the present model) can be ascribed as possible origins of the observed ion azimuthal rotation. This is the way the system stabilizes. For completeness, in Fig. 12.b, the axial component of the IVDF at the exit plane $z=z_{ep}$ is also reported (red curve in linear scale on the right). The temperature of the beam peak is close to the neutral temperature T_N at which the ions are formed. The IVDF at the exit plane will be used in the companion paper [39] on NFP simulation, as input data to inject ions from the discharge channel.

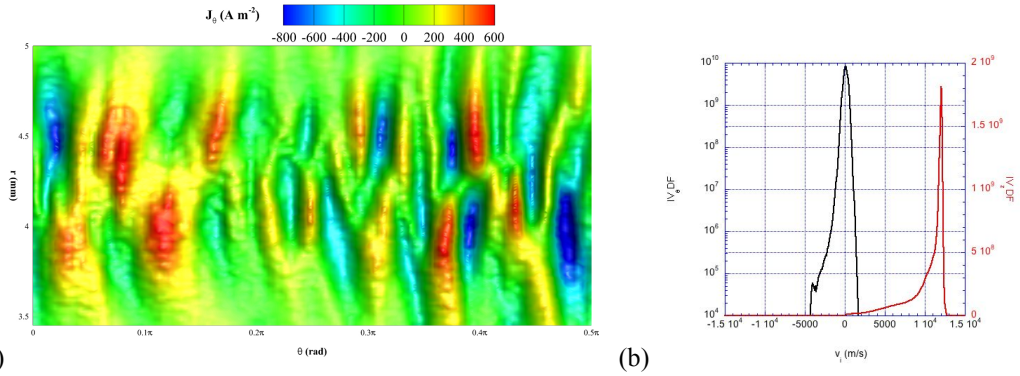

(a) (b)

Fig. 12 – a) Two-dimensional maps in the (r,θ) plane at $z=z_{acc}$ of the azimuthal component of the Xe^+ ion current density $j_{Xe+,\theta}$ (A/m^2) at the instant of maximum wave amplitude. b) Xe^+ Ion velocity distribution function for azimuthal (black) and axial (red) components. The azimuthal component of IVDF has been computed at $z=z_{acc}$, while the axial component at the exit plane $z=z_{ep}$.

Conclusions

We have studied the Hall thruster discharge channel by a three-dimensional electrostatic Particle-in-Cell model by using the expedient of a geometrical scaling. Thanks to the contemporary presence of all the three dimensions, the strong correlation between azimuthal drift instability, floating lateral walls boundary conditions and axial convection has been pointed out. In particular, the radial closure imparts a multidimensional character and a transition to nonmagnetic ion acoustic instability. The ExB drift instability shows maximum amplitude phases interspersed with quiescent phases. During the instability, the wave moves back and forth in the azimuthal direction resulting in an almost standing wave. The instability

saturates via ion heating and trapping leading to an instability amplitude oscillation whose period corresponds to the ion convection time. Finally, the role of secondary electron emission (thermostatic mechanism) as additional saturation mechanism of the electron drift instability has been highlighted.
In the future, the inclusion of the near-field region of the plume and reduction of the scaling factor will be implemented in the present model in order to assess the influence of the approximations done. In addition, on the basis of recent model results [26, 30, 33], the number of particles per cell used will be incremented to reduce as much as possible the effects of intrinsic noise and numerical heating typical of particle-based methodologies.

Knowledgments

This work was supported in part by the ApuliaSpace Project under Grant PON03PE_00067_6. The authors would also like to acknowledge participants of the ***E***x***B*** 2017 workshop https://exb-2017.sciencesconf.org/)

References

[1] A. I. Morozov and V. V. Savelyev, in Reviews of Plasma Physics, edited by B. B. Kadomstev and V. D. Shafranov (Kluwer Academic/Plenum Publishers, New York, 2000), Vol. 21.

[2] V. V. Zhurin, H. R. Kaufman, and R. S. Robinson, *Plasma Sources Sci. Technol.* **8,** R1 (1999).

[3] J.-P. Boeuf, *J. Appl. Phys.* **121**, 011101 (2017).

[4] C. R. Koppel, and D. Estublier, in *29th International Electric Propulsion Conference*, (The Electric Rocket Propulsion Society, Princeton, 2005), paper IEPC-05–119.

[5] N. B. Meezan, W. A. Hargus, Jr., and M. A. Cappelli, *Phys. Rev. E* **63**, 026410 (2001).

[6] T. Lafleur, S. D. Baalrud, and P. Chabert, *Phys. Plasmas* **23**, 053503 (2016).

[7] T. Lafleur, S. D. Baalrud, and P. Chabert, *Plasma Sources Sci. Technol.* **26**, 024008 (2017).

[8] J. C. Adam, A. Héron, and G. Laval, *Phys. Plasmas* **11**, 295 (2004).

[9] A. Ducrocq, J. C. Adam, A. Héron, and G. Laval, *Phys. Plasmas* **13**, 102111 (2006).

[10] M. Keidar, I. I. Beilis, *IEEE Trans. Plasma Sci.* **34(3)**, 804 (2006).

[11] F. Taccogna, S. Longo, M. Capitelli, R. Schneider, *Contr. Plasma Phys.* **48(4)**, 375 (2008).

[12] Y. Raitses, I. D. Kaganovich, A. Khrabrov, D. Sydorenko, N. J. Fisch, and A. Smolyakov, *IEEE Trans. Plasma Sci.* **39(4)**, 995 (2011).

[13] F. Taccogna, S. Longo, M. Capitelli, R. Schneider, *Appl. Phys. Lett.* **94**, 251502 (2009).

[14] M. D. Campanell, A. V. Khrabrov, and I. D. Kaganovich, *Phys. Plasmas* **19**, 123513 (2012).

[15] A. I. Smolyakov, W. Frias, I. D. Kaganovich, and Y. Raitses, *Phys. Rev. Lett.* **111**, 115002 (2013).

[16] W. Frias, A. I. Smolyakov, I. D. Kaganovich, and Y. Raitses, *Phys. Plasmas* **21**, 062113 (2014).

[17] I. J. Mikellides, and I. Katz, *Phys. Rev. E* **86**, 046703 (2012).

[18] J. Bareilles, G. J. M. Hagelaar, L. Garrigues, C. Boniface, J. P. Boeuf, and N. Gascon, *Phys. Plasmas* **11(6)**, 3035 (2004).

[19] J. W. Koo, and I. D. Boyd, *Phys. Plasmas* **13**, 033501 (2006).

[20] F. I. Parra, E. Ahedo, J. M. Fife, and M. Martínez-Sánchez, *J. Appl. Phys.* **100**, 023304 (2006).

[21] L. Garrigues, J. Pérez-Luna, J. Lo, G. J. M. Hagelaar, J. P. Boeuf, and S. Mazouffre, *Appl. Phys. Lett.* **95**, 141501 (2009).

[22] L. Garrigues, S. Mazouffre, and G. Bourgeois, *J. Appl. Phys.* **111**, 113301 (2012).

[23] D. Tskhakaya, K. Matyash, R. Schneider, F. Taccogna, *Contr. Plasma Phys.* **47(8-9)**, 563 (2007).

[24] J.-P. Boeuf, *Front. Phys.* **2**, 74 (2014).

[25] T. Lafleur, S. D. Baalrud, and P. Chabert, *Phys. Plasmas* **23**, 053502 (2016).

[26] S. Janhunen, A. Smolyakov, O. Chapurin, D. Sydorenko, I. Kaganovich, and Y. Raitses, *Phys. Plasmas* **25**, 011608 (2018).

[27] F. Taccogna, R. Schneider, S. Longo, and M. Capitelli, *Plasma Sources Sci. Technol.* **17**, 024003 (2008).

[28] A. Héron and J. C. Adam, *Phys. Plasmas* **20**, 082313 (2013).

[29] V. Croes, T. Lafleur, Z. Bonaventura, A. Bourdon, and P. Chabert, *Plasma Sources Sci. Technol.* **26**, 034001 (2017).

[30] K. Hara, and S. Cho, *35th International Electric Propulsion Conference* (The Electric Rocket Propulsion Society, Atlanta, GE, 2017), paper no. IEPC-2017-495.
[31] P. Coche and L. Garrigues, *Phys. Plasmas* **21**, 023503 (2014).
[32] T. Lafleur and P. Chabert, *Plasma Sources Sci. Technol.* **27**, 015003 (2018).
[33] J. P. Boeuf, and L. Garrigues, submitted to *Phys. Plasmas* (2018).
[34] S. Tsikata, C. Honoré, N. Lemoine, and D. M. Grésillon, *Phys. Plasmas* **17**, 112110 (2010).
[35] A. Lazurenko, G. Coduti, S. Mazouffre, and G. Bonhomme, *Phys. Plasmas* **15**, 034502 (2008).
[36] S. Tsikata, N. Lemoine, V. Pisarev, and D. M. Gresillon, *Phys. Plasmas* **16**, 033506 (2009).
[37] M. Hirakawa, and Y. Arakawa, *24th International Electric Propulsion Conference* (The Electric Rocket Propulsion Society, Moscow, 1995), paper no. IEPC-1995-164.
[38] M. Hirakawa, and Y. Arakawa, *32nd AIAA/ASME/SAE/ASEE Joint Propulsion Conference* (American Institute of Aeronautics and Astronautics, Lake Buena Vista, FL, 1996) paper no. 1996-3195.
[39] F. Taccogna et, and P. Minelli, submitted to *Phys. Plasmas*, (2018).
[40] E. Y. Choueiri, *Phys. Plasmas* **8**, 1411 (2001).
[41] F. Taccogna, S. Longo, M. Capitelli, R. Schneider, *Phys. Plasmas*, **12,** 43502 (2005).
[42] J. Duras, K. Matyash, D. Tskhakaya, O. Kalentev, and R. Schneider, *Contrib. Plasma Phys.* **54(8)**, 697 (2014).
[43] G. L. Delzanno, and E. Camporeale, *J. Comp. Phys.* **253**, 259 (2013).
[44] L. B. King, *29th International Electric Propulsion Conference* (The Electric Rocket Propulsion Society, Princeton NJ, 2005), paper no. IEPC-2005-258.
[45] F. Taccogna, S. Longo, M. Capitelli, R. Schneider, *Phys. Plasmas*, **12,** 053502, 2005.
[46] J. C. Adam, J. P. Boeuf, N. Dubuit, M. Dudeck, L. Garrigues, D. Gresillon, A. Heron, G. J. M. Hagelaar, V. Kulaev, N. Lemoine, S. Mazouffre, J. Perez Luna, V. Pisarev, and S. Tsikata, *Plasma Phys. Control. Fus.* **50**, 124041 (2008).
[47] K. Hara, M. J. Sekerak, I. D. Boyd, and A. D. Gallimore, *J. Appl. Phys.* **115**, 203304 (2014).
[48] M. J. Sekerak, B. W. Longmier, A. D. Gallimore, D. L. Brown, R. R. Hofer, and J. E. Polk, *IEEE Trans. Plasma Sci.* **43(1)**, 72 (2015).
[49] A. Lazurenko, T. Dudok de Wit, C. Cavoit, V. Krasnoselskikh, A. Bouchoule, and M. Dudeck, *Phys. Plasmas* **14**, 033504 (2007).
[50] L. Wei, K. Han, Ch. Wang, Ch. Zhang, and D. Yu, *Contrib. Plasma Phys.* **52**, 761 (2012).
[51] A. W. Smith, and M. A. Cappelli, *Phys. Plasmas* **16**, 073504 (2009).
[52] S. Balay, S. Abhyankar, M. Adams, J. Brown, P.B.K. Buschelman, L. Dalcin, V. Eijkhout, W.D. Gropp, D. Kaushik, M.G. Knepley, L.C. McInnes, K. Rupp, B.F. Smith, S. Zampini, H. Zhang, Portable, extensible toolkit for scientific computation, http://www.mcs.anl.gov/petsc (2015).
[53] M. A. Furman, and M. T. F. Pivi, *Phys. Rev. Special Topics–Accel. and Beams* **5**, 124404 (2002).
[54] M. Belhaj, K. Guerch, P. Sarrailh, and N. Arcis, *Nucl. Instrum. Meth. Phys. Res. B* **362**, 163 (2015).
[55] F. Taccogna, *J. Plasma Phys.* **81(1)**, 305810102 (2015).
[56] J. Szabo, N. Warner, M. Martinez-Sanchez, and O. Batishchev, *J. Prop. & Pow.* **30(1)**, 197 (2014).

[57] I. Katz, R. Hofer, and D. Goebel, *IEEE Trans. Plasma Sci.* **36(5)**, 2015 (2008).
[58] L. K. Jha, O. P. Santosh Kumar, Roy, and P. Kumar, *Phys. Scripta* **77**, 015304 (2008).
[59] E. W. Bell, N. Djuric, and G. H. Dunn, *Phys. Rev. A* **48(6)**, 4286 (1993).
[60] I. Katz, A. L. Ortega, B. A. Jorns, and I. G. Mikellides, 52nd AIAA/ASME/SAE/ASEE Joint Propulsion Conf. (Salt Lake City, UT: American Institute of Aeronautics and Astronautics, 2016) AIAA-2016-4534.
[61] J. Cavalier, N. Lemoine, G. Bonhomme, S. Tsikata, C. Honoré, and D. Grésillon, *Phys. Plasmas* **20**, 082107 (2013).
[62] M. K. Scharfe, C. A. Thomas, D. B. Scharfe, N. Gascon, M. A. Cappelli, and E. Fernandez, *IEEE Trans. Plasma Sci.* **36(5)**, 2058 (2008).
[63] A. A. Litvak, and N. J. Fish, *Phys. Plasmas* **11(4)**, 1379 (2004).
[64] A. A. Litvak, Y. Raitses, and N. J. Fish, *Phys. Plasmas* **11(4)**, 1701 (2004).
[65] R. A. Martinez, H. Dao, and M. L. R. Walker, *J. Prop. & Pow.* **30(1)**, 209 (2014).
[66] S. Barral, K. Makowski, Z. Peradzyński, and M. Dudeck, *Phys. Plasmas* **12**, 073504 (2005).
[67] S. Mazouffre, F. Dubois, L. Albarède, D. Pagnon, M. Touzeau, and M. Dudeck, IEEE Proceedings of the International Conference on Recent Advances in Space Technologies RAST03, 69 (2003).
[67] S. Tsikata, A. Héron, and C. Honoré, *Phys. Plasmas* **24**, 053519 (2017).
[68] E. Fernandez, M. K. Scharfe, C. A. Thomas, N. Gascon, and M. A. Cappelli, *Phys. Plasmas* **15**, 012102 (2008).
[70] M. Lampe, W. Manheimer, J. McBride, J. Orens, R. Shanny, and R. Sudan, *Phys. Rev. Lett.* **26**, 1221 (1971).